Supporting Information

Palva et al. 10.1073/pnas.1216855110

SI Materials and Methods

Magneto-/Electroencephalography Recordings and Source Reconstruction. As earlier (1, 2), for each subject, the FreeSurfer software (http://surfer.nmr.mgh.harvard.edu/) was used for automatic volumetric segmentation of the MRI data, reconstruction of white-gray matter and pial surfaces, flattening of complete cut surfaces, and cortical parcellation and labeling with the Destrieux atlas (3–5). MNE software (www.martinos.org/mne/) was used to create three-layer boundary element conductivity models and cortically constrained source models with fixed-orientation dipoles at 7-mm spacing oriented orthogonal to the cortical surface. MNE software also was used for magneto-/electroencephalography (M/EEG)–MRI colocalization and for the preparation of the forward and inverse operators (6–8).

M/EEG signals, $Y(t)$, are related to the source activity by relation $Y(t) = \Gamma X(t) + N(t)$, where Γ is the lead field matrix (forward operator) that relates the source dipole strengths to the sensor level data, $X(t)$ is the source dipole data, and $N(t)$ is noise. To obtain $X(t)$ from the measured $Y(t)$, we used a minimum-norm estimator, such that $X(t) = MY(t) = R\Gamma^T(\Gamma R\Gamma^T + \lambda^2\chi)$, where M is the inverse operator, R the source covariance matrix, λ^2 a regularization parameter, and χ the noise covariance matrix (6–8).

After exclusion of environmental and physiological artifacts, the recorded M/EEG data were filtered (*Materials and Methods*) and transformed to time series of ∼7,000 source dipoles with $X(t) = MY(t)$ and then collapsed to time series in a cortical parcellation, i.e., a set of cortical patches, each of which is a set of source vertices (1, 2). Here, we used a parcellation strategy aiming to minimize spurious interactions between patch time series and, to this end, searched iteratively for each individual a parcellation that maximized the correlation between simulated and inverse modeled time series for each given patch (fidelity, ξ) and minimized the correlation between the inverse modeled time series of each patch with the simulated time series of other patches (infidelity, ψ). This fidelity-optimization approach was applied with a selection criterion of maximal $0.7^*\xi + 0.3^*(1 - \psi)$ to an anatomical parcellation of 400 patches that were derived from the Destrieux atlas by iteratively splitting the patches that had the largest size in the subject population along the axis (anterior-posterior, lateral-medial, ventral-dorsal) with largest mean variance (1, 2). The iterative fidelity optimization was performed, in short, so that patch and source vertex time series were simulated with each source vertex sharing the time series of the patch owning it. The source vertex time series then were forward and inverse modeled, and for each patch, the vertices yielding the maximal value of selection criterion were selected. ξ and ψ were calculated at each step of the iterative selection process between the simulated patch time series and a weighted average of the time series of the vertex constellation tested. The inverse modeled vertex data were collapsed into patch data by obtaining the time series for each patch as an average of the time series of vertices in that patch, weighted by $|\mathrm{Re}(\xi)|$.

Neuronal long-range temporal correlation (LRTC) and avalanche analyses in individual subjects were performed on time series in the 400-patch parcellation. Group statistics and visualization of brain–behavior correlations were performed in the Destrieux parcellation with the scaling exponent of each Destrieux parcellation patch obtained by averaging the exponents of the corresponding subpatches.

Estimation of Scaling Laws for LRTCs. Detrended fluctuation analysis (DFA) was applied to estimate the scaling laws for LRTCs. DFA is a two-stage procedure: In the first stage, time series $X(k)$ is normalized to zero mean and integrated, $y(k) = \sum_{i=1}^{k}[X(i) - \langle X\rangle]$, then segmented into time windows of various sizes Δt. In the second stage, each segment of integrated data is locally fitted to a linear function $y_{\Delta t}(k)$ and the mean-squared residual $F(\Delta t)$ is computed:

$$F(\Delta t) = \sqrt{\frac{1}{N}\sum_{k=1}^{N}[y(k) - y_{\Delta t}(k)]^2},$$

where N is the total number of data points.

The scaling law exponent β is defined as the slope of linear regression of the function $F(\Delta t)$ in log–log coordinates, estimated using a least-squares algorithm.

Estimation of Behavioral and Neuronal DFA. To assess the LRTCs, DFA was applied to the behavioral sequence of Hits and Misses, neuronal oscillation amplitude envelopes, and the time series of neuronal avalanches. Unlike the magnetoencephalography (MEG) data, the behavioral time series of Hits/Misses were sparsely and irregularly sampled because of the variability in interstimulus intervals that were distributed uniformly between 1.5 s and 6 s (mean 3.75 s). The behavioral time series hence were linearly interpolated into a time series of 0s and 1s with a 10-Hz sampling rate. To discard any possible effects of this interpolation on the scaling law exponents, only DFA time windows between 4 and 400 s were used in the regression. To consolidate that the behavioral LRTCs could not be explained by a random process, we shuffled the Hit–Miss time series and reproduced the resampling and DFA estimation for 1,000 iterations. Of 56 behavioral time series, 44 yielded LRTC exponents greater than the mean on surrogates ($P < 10^{-5}$, binomial test), showing that the behavioral LRTCs were a robust phenomenon. The scaling exponents were not correlated with hit rate ($P > 0.5$), even though for random Hit–Miss sequences, very low hit rates impose a positive bias. To assess the scaling exponents of the neuronal LRTCs, DFA was applied to the amplitude envelope of the filtered signal for each cortical patch and frequency band. For consistency with the behavioral DFA analysis and to exclude the possibility that short-range correlations or filtering biased the neuronal LRTC exponents, we used the same 4–400-s range for regression of the DFA slope. All neuronal LRTC exponents were greater than the 99.99 percentile of surrogates estimated as in ref. 9 and, hence, highly significant.

Estimation of Scaling Laws for Neuronal Avalanches. Broad-band filtered neuronal activity time series of each cortical patch were normalized by subtracting the mean and dividing by SD. Then the time series were down-sampled to 300 Hz to achieve a time bin size comparable with prior experiments with local field potential (LFP) recordings. Each patch time series was transformed to a binary point process by detecting positive and negative peaks above a threshold of three SDs, and setting the samples corresponding to peak latencies to ones ("1"). These binary sequences then were summed across cortical patches to create the avalanche time series (Fig. 1*F*). Zeros in this time series constitute the interavalanche "waiting" periods and sequences of consecutive values above 0 an avalanche. The avalanches were described in terms of their lifetimes, given by the durations in milliseconds, and sizes, given by the total number of peaks. To estimate the avalanche lifetime and size distributions (10), the histogram ap-

proach was used. Sizes of the histogram bins were selected from power-spaced series (1.8^m, m = 1, …, 9). A complementary characteristic, the κ-index, for neuronal avalanches was introduced by Shew et al. (11). This nonparametric measure quantifies the difference between an experimental cumulative density function (CDF) of the avalanche size, $F(b_k)$, and the theoretical reference CDF, $F^{NA}(b_k)$, which is a power-law function with the theoretically expected exponent −3/2:

$$\kappa = 1 + \frac{1}{m}\sum_{k=1}^{m}\left(F^{NA}(b_k) - F(b_k)\right),$$

where b_k are the power-spaced avalanche sizes with, in our implementation, the base of 1.8 (1.8^m) and m = 1, …, 9. κ-index values at around 1 are characteristic of systems in a critical state, whereas values below and above 1 suggest sub- and supercritical states, respectively.

Simulations and Validation. Forward-inverse modeling, which uses spatiotemporal information of the M/EEG data, potentially may induce the spatial and temporal correlation in neuronal time series. To verify that scaling law exponents are not affected by modeling, we assessed the scaling exponents for simulated data. Random signals with uniform probability density function (PDF) were generated for each cortical patch, then Morlet wavelets with central frequency of 10 Hz and broad-band filters were applied to patch time courses. Cortical patches were mapped to source space (~7,000 sources), then forward and inverse operators were applied sequentially. Finally, the signals were mapped back to cortical patch space, and scaling exponents were computed. We used the same approach to assess the impact of noise generated by the empty scanner.

SI Note. It is important to note that the present data relate only indirectly to 1/*f* scaling in frequency spectra. The scaling in the low-frequency end of the classical power spectra is biased by the conductive properties of brain tissue (12), and the signals in this frequency regime may have several incompletely understood neurophysiological or hemodynamic sources (13). These confounders influence the scaling laws of the power spectra obtained directly from real-valued M/EEG signals, but are not relevant for the amplitude envelopes of narrow-band neuronal oscillations studied here. Our LRTC analyses focus on slow fluctuations in the amplitude envelopes of fast neuronal oscillations that reflect the dynamics of more specific neuronal processes and yield (amplitude) scaling laws that are not influenced by the passage of electrical and magnetic fields in brain tissue (12).

1. Palva JM, Monto S, Kulashekhar S, Palva S (2010) Neuronal synchrony reveals working memory networks and predicts individual memory capacity. *Proc Natl Acad Sci USA* 107(16):7580–7585.
2. Palva S, Kulashekhar S, Hämäläinen M, Palva JM (2011) Localization of cortical phase and amplitude dynamics during visual working memory encoding and retention. *J Neurosci* 31(13):5013–5025.
3. Dale AM, Fischl B, Sereno MI (1999) Cortical surface-based analysis. I. Segmentation and surface reconstruction. *Neuroimage* 9(2):179–194.
4. Fischl B, Sereno MI, Dale AM (1999) Cortical surface-based analysis. II: Inflation, flattening, and a surface-based coordinate system. *Neuroimage* 9(2):195–207.
5. Fischl B, et al. (2002) Whole brain segmentation: automated labeling of neuro anatomical structures in the human brain. *Neuron* 33(3):341–355.
6. Hämäläinen MS, Sarvas J (1989) Realistic conductivity geometry model of the human head for interpretation of neuromagnetic data. *IEEE Trans Biomed Eng* 36(2): 165–171.
7. Hämäläinen MS, Ilmoniemi RJ (1994) Interpreting magnetic fields of the brain: Minimum norm estimates. *Med Biol Eng Comput* 32(1):35–42.
8. Lin FH, Belliveau JW, Dale AM, Hämäläinen MS (2006) Distributed current estimates using cortical orientation constraints. *Hum Brain Mapp* 27(1):1–13.
9. Linkenkaer-Hansen K, Nikouline VV, Palva JM, Ilmoniemi RJ (2001) Long-range temporal correlations and scaling behavior in human brain oscillations. *J Neurosci* 21(4):1370–1377.
10. Beggs JM, Plenz D (2003) Neuronal avalanches in neocortical circuits. *J Neurosci* 23(35):11167–11177.
11. Shew WL, Yang H, Petermann T, Roy R, Plenz D (2009) Neuronal avalanches imply maximum dynamic range in cortical networks at criticality. *J Neurosci* 29(49): 15595–15600.
12. Dehghani N, Bédard C, Cash SS, Halgren E, Destexhe A (2010) Comparative power spectral analysis of simultaneous elecroencephalographic and magnetoencephalographic recordings in humans suggests non-resistive extracellular media. *J Comput Neurosci* 29(3):405–421.
13. Palva JM, Palva S (2012) Infra-slow fluctuations in electrophysiological recordings, blood-oxygenation-level-dependent signals, and psychophysical time series. *Neuroimage* 62(4):2201–2211.

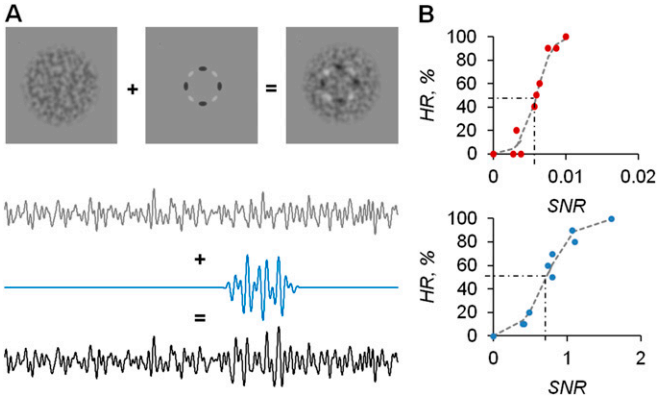

Fig. S1. Signal-to-noise ratio (SNR) of the visual and auditory stimuli was adjusted for each subject in a calibration session before the experiment. (*A*) Visual stimuli (circular pattern) lasted 50 ms and were superimposed on a continuous, very slowly moving Perlin noise background. The auditory stimuli were dual-frequency (115- and 185-Hz) Hanning-windowed sinusoidal signals lasting 50 ms and were superimposed on continuous Poisson noise (50–350 Hz). (*B*) Intensities of visual and auditory stimuli were calibrated before the experiment to yield an initial hit rate of ~50%. Auditory and visual stimuli were detected with equal probabilities ($P > 0.34$) in uni- and bimodal experiments. The mean final hit rates in the unimodal tasks (mean of auditory and visual hit rates: 0.44 ± 0.04, mean ± SEM) were significantly ($P < 0.05$) higher than the final hit rates in the bimodal task (0.36 ± 0.04).

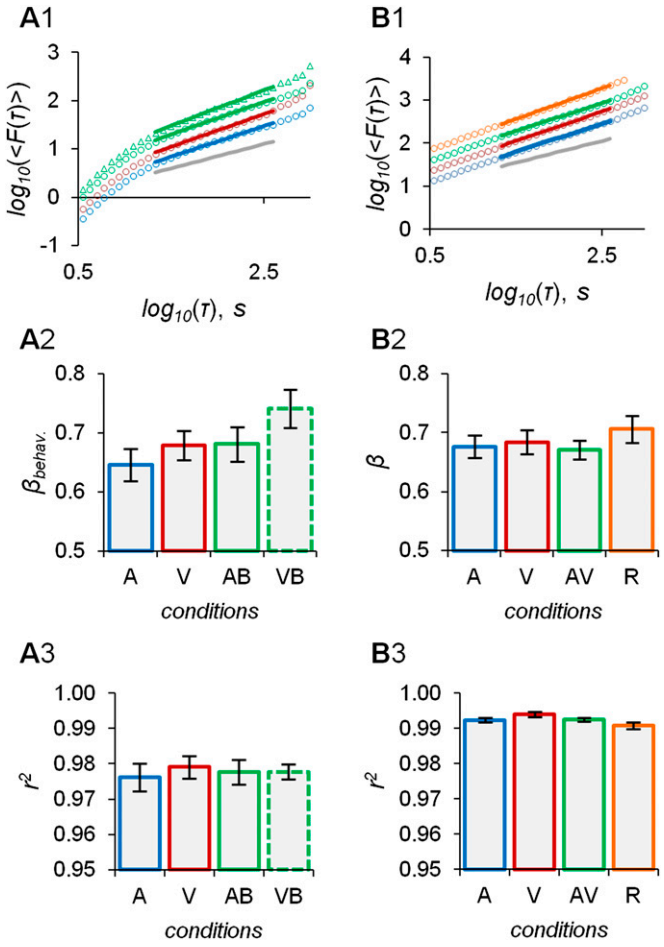

Fig. S2. Behavioral data, as well as task- and resting-state neuronal data, reveal robust scaling laws and significant task effects. (*A1*) DFA of behavioral time series (averaged across subjects). Blue, unimodal auditory; red, unimodal visual; green ○, bimodal auditory; green △, bimodal visual. Lines indicate best-fit linear regression in the time range from 4 to 400 s. (*A2*) Comparisons of the scaling exponents across subjects and conditions with a two-way ANOVA revealed an effect of both sensory modality ($P < 0.03$, *F*-test) and task ($P < 0.02$, *F*-test), but not an interaction between modality and task. Error bars indicate the SEM of scaling exponents across subjects. Note that within-subject means were subtracted before ANOVA to remove the contribution of large interindividual variability therein (*Results*). A, auditory; B, bimodal; V, visual. (*A3*) Mean ± SEM r^2 values for the goodness of fit of the linear regression on behavioral DFAs. (*B1*) DFA of task- and resting-state 10-Hz neuronal oscillations (averaged across subjects). Blue, auditory; red, visual; green, audiovisual; orange, resting-state. Colored lines indicate best-fit linear regression in the time range from 4 to 400 s; gray line is the DFA of phase-randomized surrogate data with an exponent of ∼0.5; all individuals had exponents above this value. (*B2*) Comparisons of the neuronal scaling exponents between conditions with one-way ANOVA revealed an effect of task ($P < 0.008$, *F*-test; see note on *A2*), whereas the effect of task (all three conditions) vs. resting state was not significant ($P > 0.11$, *F*-test). (*B3*) Mean ± SEM r^2 values for the goodness of fit of the linear regression on neuronal DFAs. Systematic variability of both the LRTC and avalanche scaling exponents among different task conditions (see also Fig. S3) yields a complementary view on the putative significance of scaling laws in neuronal dynamics. Comparable effects were observed earlier with MEG and functional MRI between task and rest conditions (1, 2). In these data, the scaling exponents were not suppressed from resting-state levels during task performance, which likely is attributable to the threshold-stimulus detection task paradigm, in which the stimulus-evoked disruption of ongoing dynamics is minimal. The task effects show that rather than being a stationary property of individual nervous systems, the scaling exponents are malleable, dynamic, and dependent on brain states in time scales from minutes to tens of minutes. In other words, if the scaling exponents are taken as indicators of the brain operating near a critical state, then this operating point, even in the healthy brain, may flexibly fluctuate in the neighborhood of the critical regime.

1. Linkenkaer-Hansen K, Nikulin VV, Palva JM, Kaila K, Ilmoniemi RJ (2004) Stimulus-induced change in long-range temporal correlations and scaling behaviour of sensorimotor oscillations. *Eur J Neurosci* 19(1):203–211.
2. He BJ (2011) Scale-free properties of the functional magnetic resonance imaging signal during rest and task. *J Neurosci* 31(39):13786–13795.

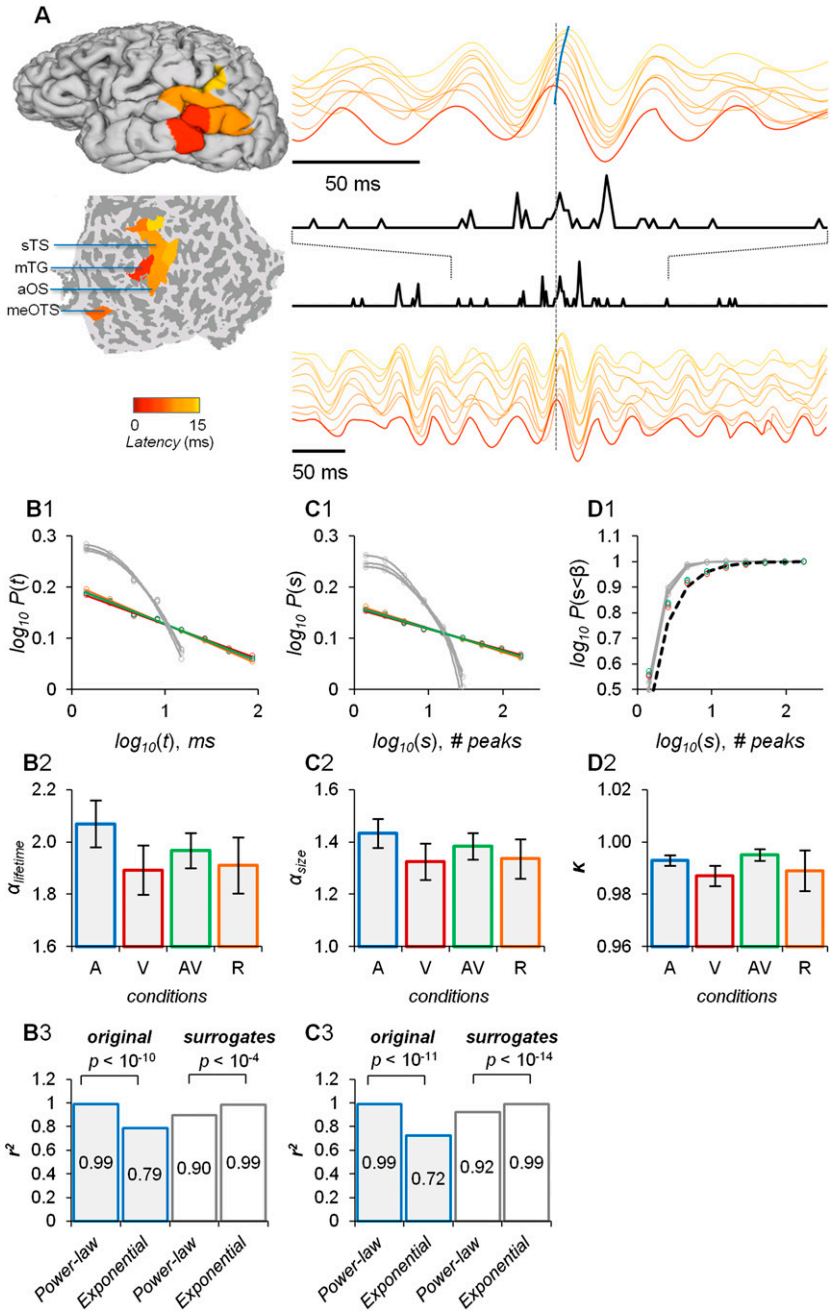

Fig. S3. Avalanche dynamics are prominent in source-reconstructed M/EEG data during both task- and resting-state conditions. (*A*) Example avalanche showing a cascade propagating in the left hemispheric occipital and temporal regions (see Fig. 1*F* for color coding). (*B1*) Lifetime distribution of avalanche dynamics is significantly different from that of surrogates obtained by random rotation of cortical patch time series, which preserves the autocorrelation structure but mixes temporal relationships between patches [gray lines, $P < 0.005$, Kolmogorov–Smirnov (KS) test; for colors, see *B2*; distributions averaged across subjects]. (*B2*) Task effect on the lifetime scaling exponents (mean ± SEM across subjects) estimated with a one-way ANOVA was significant ($P < 0.002$, *F*-test), but the effect of task vs. rest, R, was not ($P > 0.16$, *F*-test). A, auditory; AV, audiovisual, V, visual. (*B3*) Avalanche lifetime distributions of original data of individual datasets were fit (r^2 on the *y* axis) by power laws better than by exponentials ($P < 10^{-10}$, *t*-test), whereas the surrogate data were represented better by exponentials than by power laws ($P < 10^{-4}$, *t*-test). This observation was fully reproduced when using the maximum likelihood approach (1) (maximum likelihood ratio test for the original data being better described by a power law than by an exponential; $P < 0.0001$). (*C1*) Size distributions of avalanches showed similar characteristics as lifetime distributions (*B*) and were different from surrogate data (gray lines, $P < 0.002$, KS test). (*C2*) One-way ANOVA again revealed a task effect ($P < 0.03$, *F*-test) but no difference between task and rest conditions ($P > 0.22$, *F*-test). (*C3*) The size distributions of original data were better fit by power laws than by exponentials ($P < 10^{-11}$, *t*-test), and vice versa for surrogate data ($P < 10^{-14}$, *t*-test); this finding also was corroborated with the maximum likelihood analysis (as in *B*; $P < 0.0001$) (*D1* and *D2*) We used the κ-index as an additional measure of the size distribution scaling. The cumulative distribution function (CDF) for observing an avalanche with a given size was well fit with the CDF of the power-law function $G(\boldsymbol{s}) = s^{-3/2}$ (dashed line), in agreement with previous studies on avalanche dynamics in nonhuman data (2).

1. Klaus A, Yu S, Plenz D (2011) Statistical analyses support power law distributions found in neuronal avalanches. *PLoS ONE* 6(5):e19779.
2. Petermann T, et al. (2009) Spontaneous cortical activity in awake monkeys composed of neuronal avalanches. *Proc Natl Acad Sci USA* 106(37):15921–15926.

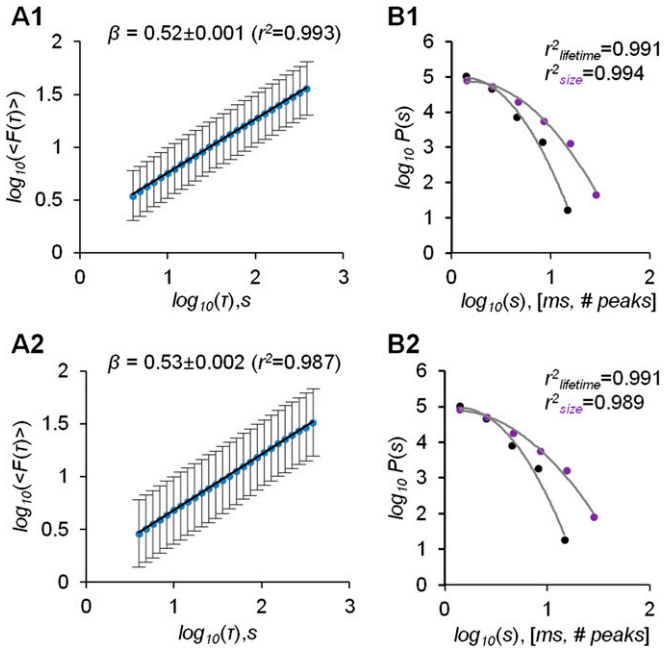

Fig. S4. Artificial LRTC or power-law avalanche dynamics are not produced by residual environmental or instrument noise, the mixing of neuronal signals at the scalp level, or the source reconstruction methods. We used forward modeling to simulate virtual M/EEG recordings of uncorrelated brain activity and identically preprocessed empty-room MEG recordings to probe environmental and instrument noise. These M/EEG and MEG datasets then were inverse modeled with the inverse operators and methods used elsewhere in the data analyses as well. The 10-Hz LRTC scaling exponents of both (*A1*) forward-modeled data ($\beta = 0.52 \pm 0.001$) and (*A2*) those recorded by an empty scanner ($\beta = 0.53 \pm 0.002$) were close to the theoretical DFA scaling exponent for white noise ($\beta = 0.5$). The avalanche lifetime and size distributions are exponentials for both (*B1*) forward- and inverse-modeled white noise ($r^2_{lifetime} = 0.991$, $r^2_{size} = 0.994$) and (*B2*) for inverse-modeled scanner noise ($r^2_{lifetime} = 0.991$, $r^2_{size} = 0.989$).

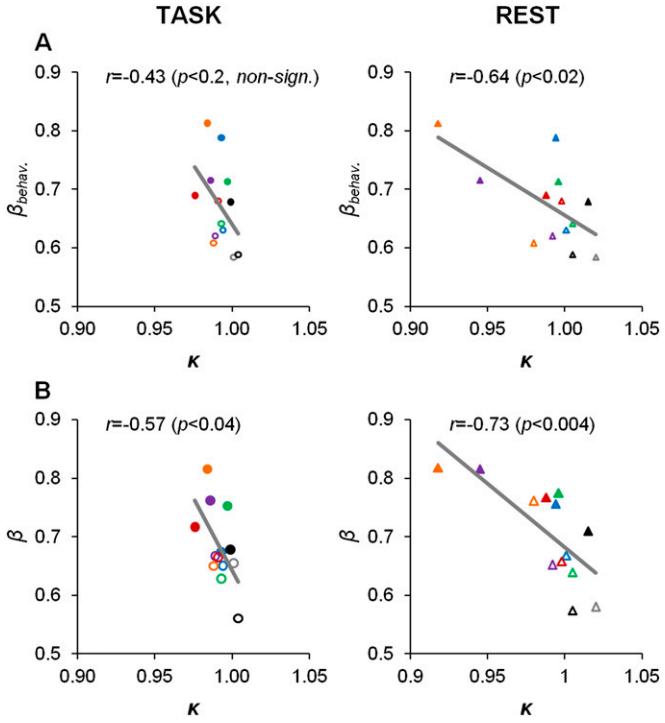

Fig. S5. As in Fig. 2, the scaling-law exponents of behavioral and neuronal LRTCs also are correlated with avalanche κ-indices (*A* and *B*). Note the consistency of the results within subjects in task (circles) and rest (triangles) conditions; unique colors/fills indicate individual subjects.

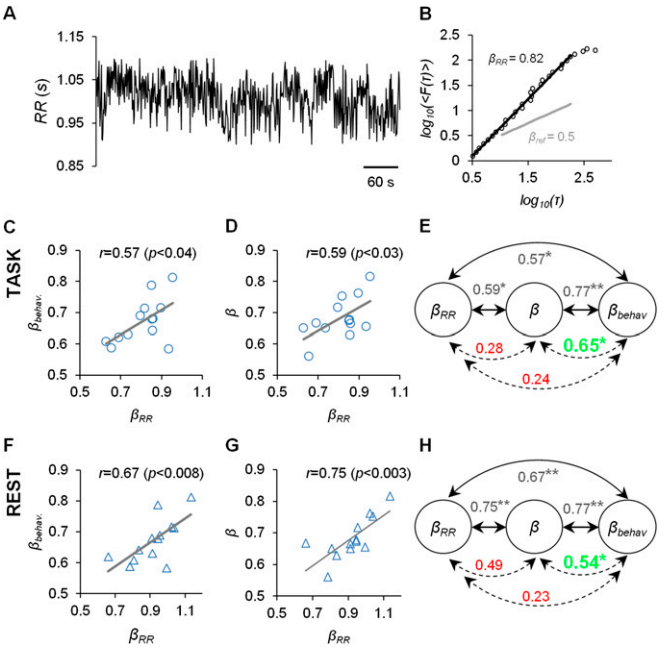

Fig. S6. Dynamics of interheartbeat (RR) intervals are scale-free and their scaling exponents are correlated during both task and rest with behavioral and neuronal exponents so that the correlation with behavior is mediated by correlation with neuronal LRTCs. (*A*) Time series of RR intervals of 10-min recording of a representative subject shows fractal-like dynamics. (*B*) DFA plot for the time series of RR intervals (*A*) reveals salient LRTCs (β_{RR}, scaling exponent of RR time series; β_{ref}, reference value for random data). (*C*) The behavioral LRTC scaling exponents, $\beta_{behav.}$, and (*D*) the LRTC scaling exponents of 10-Hz neuronal oscillations, β, were correlated with those of RR intervals across subjects ($P < 0.04$ and $P < 0.03$, respectively; Pearson correlation test) (*E*) Whereas the correlations among behavioral, neuronal, and heartbeat scaling exponents were significant, partial correlation analysis suggested that correlation of heartbeat with behavior was indirect and mediated by neuronal LRTCs. (*F–H*) RR, neuronal, and behavioral LRTC data as in *D*, *E*, and *F*, respectively. Red (not significant) and green (significant) correlation coefficients indicate the values of partial correlations and show that the correlation between neuronal and behavioral LRTC exponents remains significant when the heartbeat LRTC is factored out, but not vice versa. Gray numbers denote the pairwise correlation coefficients.

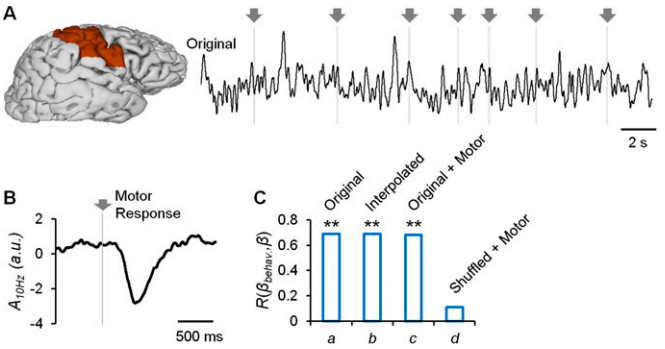

Fig. S7. Motor responses do not affect the LRTC scaling exponents of the sensorimotor cortex during task performance or their correlation with behavioral LRTCs. (*A*) Thirty-second 10-Hz oscillation amplitude fluctuations were averaged across the corresponding time series from each subarea of the bilateral sensorimotor cortex (SMC; comprising the pre- and postcentral gyri and the central sulcus of the Destrieux atlas) of a representative subject. Arrows indicate button presses. (*B*) Motor response averaged in a 0–1.5-s peri–button press time window across all button presses of the representative subject composed of a transient amplitude suppression after the button press. (*C*) To investigate the contribution of motor responses on SMC amplitude dynamics and LRTCs at the group level, we isolated for each subject the spontaneous amplitude time series of the bilateral SMC (as in *A*) and estimated the mean amplitude dynamics associated with motor responses (as in *B*). (*C*, *a*) Post hoc DFA analysis of the intact SMC amplitude time series reproduced the brain–behavior correlation of the LRTC scaling exponents ($r = 0.70$, $P < 0.006$). We then used three approaches to examine the contribution of the motor responses. (*C*, *b*) First, we removed and interpolated the amplitude time series in the time windows of the motor responses. This decreased the brain–behavior correlation only slightly ($r = 0.68$, $P < 0.007$) from the value observed for the original time series. (*C*, *c*) Second, we added mean motor responses to the original time series; if the motor responses biased the original data toward a higher correlation, it should be observed here. However, we found that this manipulation did not change the brain–behavior correlation at all ($r = 0.70$, $P < 0.006$). (*C*, *d*) Third, we used frequency-domain phase randomization to shuffle the temporal structure of the original SMC amplitude time series while maintaining an identical power spectrum; then, we superimposed the individual mean response waveform into individual response latencies. If the motor responses per se introduced an artificial brain–behavior correlation in the scaling-law exponents, it should be reproduced here. However, there was no significant correlation between the scaling exponents of these time series with those of behavior ($r = 0.11$, $P > 0.72$). These three tests thus convergently indicate that even in SMC, the motor responses do not introduce artificial brain–behavior correlations among the scaling exponents. $^{**}P < 0.01$.

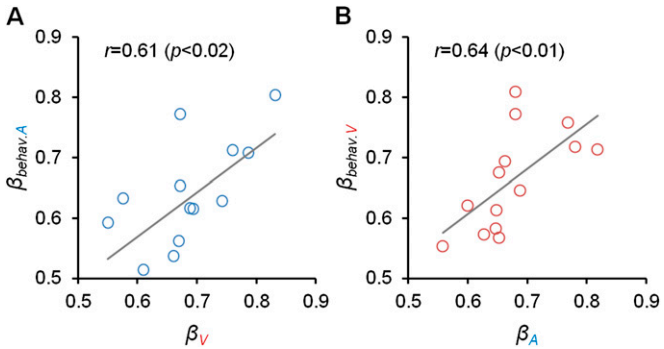

Fig. S8. Neuronal LRTCs measured during the performance of an auditory or visual task are correlated with behavioral LRTCs measured in a separate session and with the other (visual or auditory, respectively) modality. Together with the correlation of resting-state neuronal LRTCs with behavioral task-state LRTC (Fig. 2*A*), these data suggest that the scaling exponents reflect individual phenotypic brain dynamic characteristics and are relatively independent of the specific task at hand. (*A*) Scaling exponents of behavioral LRTCs in the auditory task are correlated with the neuronal scaling exponents in the visual task, and (*B*) vice versa. These plots are comparable with those in Fig. 2*A*, in which the behavioral and neuronal scaling exponents averaged across conditions are highly correlated.